Bulletin of the Seismological Society of America, 92, 1, pp. 126–137, February 2002

Time-Dependent Distributed Afterslip on and Deep below the İzmit Earthquake Rupture

by Roland Bürgmann, Semih Ergintav, Paul Segall, Elizabeth H. Hearn, Simon McClusky, Rob E. Reilinger, Heiko Woith, and Jochen Zschau

Abstract Surface deformation transients measured with the Global Positioning System during the 87 days between the 17 August 1999 İzmit earthquake and the 12 November 1999 Düzce earthquake indicate rapidly decaying aseismic fault slip on and well below the coseismic rupture. Elastic model inversions for time-dependent distributed fault slip, using a network inversion filter approach, show that afterslip was highest between and below the regions of maximum coseismic slip and propagated downward to, or even below, the base of the crust. Maximum afterslip rates decayed from greater than 2 m/yr, immediately after the İzmit earthquake to about 1.2 m/yr just prior to the Düzce earthquake. Maximum afterslip occurred below the eastern Karadere rupture segment and near the İzmit hypocenter. Afterslip in the upper 16 km decayed more rapidly than that below the seismogenic zone. These observations are consistent with a phase of rapid aseismic fault slip concentrated near the base of the seismogenic zone. Continued loading from the rapid deep afterslip along the eastern rupture zone is a plausible mechanism that helped trigger the nearby, M_w 7.2, 12 November Düzce earthquake.

Introduction

The midcrustal to lower crustal structure and rheology of major strike-slip faults continue to be topics of debate. On the basis of varying assumptions about the thermal structure, lithology, and mechanical properties of the crust and fault zone, the aseismic roots of brittle strike-slip faults are thought to (1) represent a zone of broadly distributed ductile flow (Nur and Mavko, 1974; Pollitz, 1992; Bourne *et al.,* 1998), (2) extend through much of the crust and possibly the upper mantle as narrow shear zones (Sibson, 1986; Tse and Rice, 1986; Scholz, 1988), or (3) be regions that experience both localized faulting well below the seismogenic zone and distributed ductile shear in the surrounding host rock during different times in the earthquake cycle (Furlong and Verdonck, 1994). Supporting evidence for either widely distributed or localized fault architecture in the lower crust can be found in geologic studies of exhumed fault zones (Bak *et al.,* 1975; Hanmer, 1988; Swanson, 1992), by seismic imaging (Brocher *et al.,* 1994; Henstock *et al.,* 1997; Parsons, 1998; Molnar *et al.,* 1999; Zhu, 2000), and in the interpretation of geodetic data (Prescott and Yu, 1986; Gilbert *et al.,* 1994; Bourne *et al.,* 1998; Pollitz *et al.,* 2000).

Earthquakes signal the beginning of a crustal-scale rock mechanics experiment, which can be analyzed by geodetic measurements that constrain the Earth's response. Two-dimensional model calculations show that the predicted surface deformation caused by aseismic slip or viscoelastic flow below the brittle upper crust are difficult to distinguish, both for steady interseismic deformation and postseismic deformation transients along strike-slip faults (Thatcher, 1983; Savage, 1990). However, both the temporal pattern and spatial distribution of deformation transients in response to large earthquakes continue to shed new light on the fault-zone rheology at depth. Since the early observations of postseismic deformation following the 1906 San Francisco earthquake (Thatcher, 1974, 1983), it has been recognized that these transients provide potentially useful information about crustal rheology as well as about the mechanics of fault interaction. Thus, most-recent major earthquakes have been the targets of intensified postseismic geodetic monitoring. Comparison of geodetic measurements collected over several years following the 1989 M_w 6.9 Loma Prieta earthquake (Bürgmann *et al.,* 1997; Pollitz *et al.,* 1998) and the 1994 M_w 6.6 Northridge earthquake (Donnellan and Lyzenga, 1998) with pre-earthquake displacement patterns indicate that postseismic deformation was dominated by continued slip on and above the buried coseismic ruptures. In the case of the Loma Prieta earthquake, postseismic slip rates rapidly decayed from about 8 cm/yr a few months after the event, to near 0 within 3–5 yr of the earthquake (Segall *et al.,* 2000). An early phase of rapidly decaying deformation measured with Global Positioning System (GPS) following the 1992 M 7.4 Landers earthquake can be explained as re-

sulting from accelerated postseismic slip below 10 km with an exponential relaxation time of 34 days (Shen *et al.,* 1994) or 84 days (Savage and Svarc, 1997). Using horizontal and vertical deformation data measured during the course of several years (combination of GPS and InSAR data) around the 1992 Landers earthquake rupture, Deng *et al.* (1998) and Pollitz *et al.* (2000) argue that distributed lower crustal and/or upper mantle flow are required to explain the later years of postseismic deformation.

The 17 August 1999 İzmit earthquake was the latest in a sequence of mostly westward propagating earthquakes ($M \geq 6.7$) along the North Anatolian fault (NAF) that started with the 1939 Erzincan earthquake (Toksöz *et al.,* 1979; Stein *et al.,* 1997). The İzmit earthquake itself was soon followed by the 12 November M_w 7.2 Düzce earthquake immediately to the east of the 17 August rupture (Ayhan *et al.,* 2001; Bürgmann *et al.,* 2002). This sequence of earthquakes has been interpreted in terms of static stress transfer from one earthquake triggering or advancing subsequent events (Stein *et al.,* 1997; Hubert-Ferrari *et al.,* 2000; Parsons *et al.,* 2000). In addition to coseismic stress changes, postseismic deformation transients further redistribute stress in the lithosphere and can play an important role in the loading and potential earthquake triggering on the nearby fault segments (Lehner *et al.,* 1981; Yang and Töksoz, 1981; Hearn *et al.,* 2002). Thus, a better understanding of the nature, magnitude, and temporal development of postseismic deformation should lead to improved time-dependent stress models and probabilistic earthquake forecasts.

Reilinger *et al.* (2000) and Woith *et al.* (1999) found deformation following the İzmit earthquake that greatly exceeded the displacement rates from before the earthquake. The GPS-measured velocities of 35 sites, averaged over the first 75 postseismic days, are best explained by rapid afterslip mostly below the coseismic rupture plane (Reilinger *et al.,* 2000). Afterslip appeared to be the largest on fault segments that experienced relatively little slip during the event and near and below the hypocenter. Inferred slip extended to and possibly even below the base of the crust at a depth of 30–36 km (Makris and Stobbe, 1984). In this contribution, we consider all the GPS data collected during the 87 days following the 17 August İzmit earthquake, until the 12 November Düzce earthquake, to constrain kinematic models of the spatiotemporal development of the İzmit earthquake afterslip leading up to the second event. The kinematic models serve as constraints for the finite element models of the postseismic relaxation that address the rheology of the lithosphere and fault zone and are presented in the companion article by Hearn *et al.* (2002). Hearn *et al.* (2002) also evaluate the stress changes associated with the transient deformation near the Düzce earthquake hypocenter and along the Northern Anatolian fault segments below the Marmara Sea.

GPS Measurements of Postseismic Deformation

A substantial GPS monitoring effort was underway prior to the İzmit–Düzce earthquake sequence. Many geodetic monuments in the region had been repeatedly occupied to measure strain accumulation along the NAF since as early as 1988 (Straub *et al.,* 1997; McClusky *et al.,* 2000). Six permanent, continuously operating GPS stations of the Marmara GPS monitoring network (MADT, MERT, KANT, DUMT, TUBI, and ANKR) were within the coseismic deformation field. One additional site (ULUT) was installed soon after the earthquake to begin tracking postseismic motions. Four more temporary, continuously recording GPS stations (HAMT, MURT, UCGT, and BEST) were installed in the near field within 48 hr of the main event by TUBITAK MAM (Ergintav *et al.,* 2002) (Fig. 1). Six additional sites in close proximity to the surface rupture (TASK, CAY1, ULU1, KOP1, ADA1, ADA2, and KOS1 shown in Fig. 1B) were established by 21 August by the GeoForschungsZentrum (GFZ) Potsdam and collected data until 15 October 1999 (Woith *et al.,* 1999).

We included data from 47 sites that were occupied at least twice in the 87-day period until the day of the Düzce earthquake (Fig. 1, Table 1). The GPS data were processed following standard procedures using the GAMIT/GLOBK GPS processing software (King and Bock, 1998; Herring, 1999) as described in McClusky *et al.* (2000) and Ergintav *et al.* (2001). Every day, GPS solutions were aligned to a Eurasia-fixed reference frame using generalized constraints (Dong *et al.,* 1998). Specifically, we minimized the departure from ITRF97 positions of 12–16 IGS stations in western Europe, while estimating six translation and rotation parameters in the network transformation. The average root mean square departure of the horizontal positions of the stations used in the transformation was 2.6 mm.

Coordinate time series of the continuously operating stations show that deformation rates were nonlinear in time during the postearthquake period (Fig. 2). Sites to the north of the rupture showed accelerated eastward motions, whereas the sites to the south moved westward. Overall, the displacement field resembles that of the earthquake, but the motions diminish less rapidly with distance from the rupture (Reilinger *et al.,* 2000). This is indicative of a more deeply buried or broadly distributed deformation source. The duration of the early rapid motions varies among stations, indicating that deformation is variable in both space and time. The postseismic transient deformation is punctuated by some local events (e.g., during and in the aftermath of the largest, 13 September 1999, M_w 5.8 aftershock near the hypocenter) that affect a subset of the stations (Fig. 2). The motions rapidly decayed in the İzmit–Düzce interevent period. Ergintav *et al.* (2001) estimated a relaxation time of 57 days by fitting a common exponential function to the time series of horizontal displacements of 38 GPS stations.

Network Inversion Filter Modeling of Postseismic Transient Deformation

We model the observed postseismic position time series using rectangular dislocations in an elastic, homogenous,

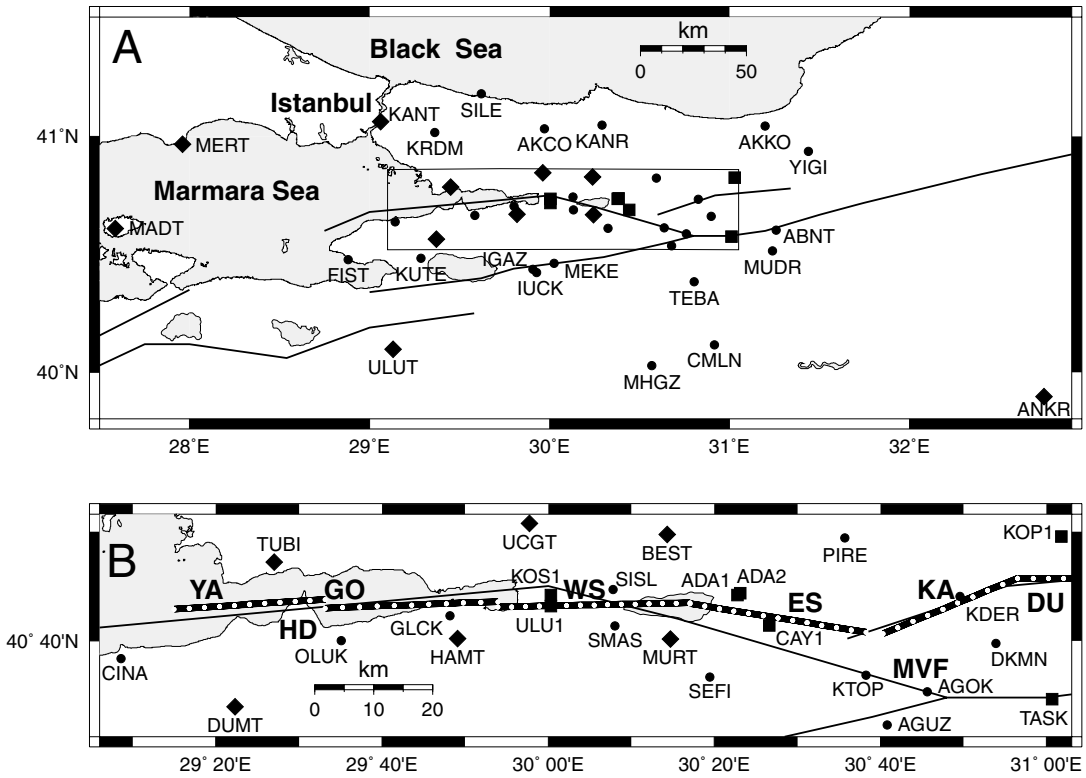

Figure 1. (A) Network map of GPS sites that were measured at least twice between the 17 August 1999 İzmit earthquake and the 12 November 1999 Düzce event. (B) Close up of (A) showing the surface trace of the vertical model fault, which encompasses the İzmit earthquake rupture as defined in Reilinger *et al.* (2000) and extends well west and east of the coseismic rupture. Diamonds indicate continuous GPS stations, squares are GFZ sites that were measured continuously from 21 August to 15 October 1999, and circles are campaign survey sites. YA, Yalova segment; HD, Hersek Delta; GO, Golcuk; WS, western Sapanca rupture segment; ES, eastern Sapanca segment; KA, Karadere fault segment; DU, Düzce fault; MVF, Mudurnu Valley fault segment.

and isotropic half-space (Okada, 1985) to represent transient strike-slip faulting following the İzmit earthquake. To better understand the distribution of postseismic fault slip in space and time, we use the network inversion filter (NIF) (Segall and Matthews, 1997; Segall *et al.*, 2000). The NIF has been developed to formally separate time-dependent deformation caused by faulting (Segall *et al.,* 2000) or volcanic deformation (Aoki *et al.,* 1999) from data error and uncorrelated random walk bench mark motions contained in a geodetic data set. The NIF can easily handle the heterogeneous distribution of GPS measurements in space and time and makes no assumptions about the parametric form (such as exponential or logarithmic decay) of the transient deformation signal (Segall *et al.*, 2000).

Some of the observed deformation results from the background secular deformation. The GPS measurements from the years prior to the İzmit earthquake show that about 25 mm/yr of the Anatolia–Eurasia motion are distributed over a ca. 100-km-wide zone across the NAF (McClusky *et al.*, 2000). The background strain field is constrained by the 1988–1997 GPS velocities in the area (McClusky *et al.*, 2000), which can be fit by a simple dislocation model of a buried east–west-striking dislocation slipping at 32 mm/yr below 24.4 km depth (Fig. 3). The geometry and slip rate of the secular dislocation model are inverted from the velocities of 45 GPS sites located between 28° E and 33° E and between 38.5° N and 42° N (Fig. 3). This model is used to compute secular motions at the postseismic network sites and is not necessarily a physically realistic model of the strain accumulation process in the region (Meade *et al.,* 2001). At each epoch, we subtract the displacements predicted by the secular model from the position observed at each postseismic site. The time series in Figure 2 include the secular contribution. During the 87-day postseismic interval, the maximum observed relative site motions amounted to as much as 120 mm (between MURT and UCGT), greatly exceeding the maximum expected background motion of 5.2 mm (22 mm/yr) across the entire network.

We assume that afterslip occurs on or surrounding (be-

Table 1
Station List

Name	Longitude	Latitude	Height	Observations	First	Last	Duration (yr)
MADT	27.5869	40.6114	0.7492	76	1999.63	1999.86	0.24
MERT	27.9617	40.9669	0.0909	68	1999.63	1999.83	0.2
KANT	29.0614	41.0608	0.155	87	1999.63	1999.86	0.24
ULUT	29.1314	40.0975	2.0889	52	1999.72	1999.86	0.15
DUMT	29.3719	40.5655	0.9293	87	1999.63	1999.86	0.24
TUBI	29.4507	40.7867	0.2217	85	1999.63	1999.86	0.24
HAMT	29.8187	40.6701	0.4491	81	1999.64	1999.86	0.23
UCGT	29.9623	40.8457	0.3952	85	1999.63	1999.86	0.24
BEST	30.2387	40.8291	0.2108	79	1999.63	1999.86	0.23
MURT	30.2453	40.6697	0.1877	84	1999.63	1999.86	0.24
ANKR	32.7585	39.8874	0.9761	87	1999.63	1999.86	0.24
ULU1	30.0054	40.7201	0.0654	46	1999.64	1999.77	0.13
KOS1	30.0057	40.7368	0.0489	46	1999.64	1999.77	0.13
ADA1	30.3797	40.7369	0.0946	23	1999.64	1999.7	0.06
ADA2	30.3853	40.7395	0.0857	24	1999.7	1999.77	0.07
CAY1	30.4439	40.69	0.0854	47	1999.64	1999.77	0.13
TASK	31.0112	40.5775	0.5876	47	1999.64	1999.77	0.13
KOP1	31.0297	40.8261	0.161	45	1999.65	1999.77	0.12
FIST	28.8818	40.4806	0.0422	3	1999.66	1999.81	0.15
CINA	29.1431	40.6395	0.17	4	1999.65	1999.81	0.16
KUTE	29.2879	40.4847	0.5008	2	1999.66	1999.72	0.05
KRDM	29.3625	41.0171	0.1568	2	1999.67	1999.82	0.16
OLUK	29.5853	40.6671	0.3915	4	1999.65	1999.82	0.16
SILE	29.6232	41.1795	0.0493	2	1999.67	1999.83	0.15
GLCK	29.8038	40.7052	0.1716	5	1999.65	1999.82	0.16
IGAZ	29.908	40.438	0.3782	5	1999.67	1999.83	0.16
IUCK	29.9289	40.4247	0.4416	4	1999.66	1999.83	0.18
AKCO	29.9731	41.0335	0.2817	3	1999.66	1999.82	0.16
MEKE	30.0264	40.4647	0.2104	3	1999.66	1999.82	0.16
SISL	30.1303	40.7453	0.1615	5	1999.65	1999.81	0.16
SMAS	30.134	40.6897	0.3045	5	1999.65	1999.81	0.16
KANR	30.2936	41.0483	0.1704	3	1999.66	1999.82	0.16
SEFI	30.3252	40.6116	0.123	4	1999.65	1999.82	0.17
MHGZ	30.5704	40.0279	0.2688	2	1999.66	1999.81	0.15
PIRE	30.5952	40.8243	0.1192	5	1999.66	1999.86	0.2
KTOP	30.6381	40.6143	0.2262	7	1999.65	1999.83	0.18
AGUZ	30.6804	40.5383	1.1972	5	1999.66	1999.73	0.07
AGOK	30.7611	40.5889	0.3322	7	1999.65	1999.83	0.19
TEBA	30.8045	40.3857	0.9849	2	1999.82	1999.86	0.04
KDER	30.8266	40.7348	0.6497	4	1999.65	1999.86	0.21
DKMN	30.8988	40.6632	1.7679	4	1999.67	1999.85	0.18
CMLN	30.9164	40.1179	0.4221	2	1999.66	1999.82	0.16
AKKO	31.1979	41.0446	0.2226	2	1999.67	1999.82	0.14
MUDR	31.2398	40.5173	0.8592	3	1999.67	1999.85	0.18
ABNT	31.2611	40.6043	1.4259	3	1999.67	1999.86	0.19
YIGI	31.4388	40.937	0.8227	6	1999.67	1999.86	0.19

low or along strike) the İzmit earthquake rupture on the vertical dislocation planes. The model fault geometry follows the trace of the mapped coseismic rupture and includes the Yalova segment under the İzmit Bay to the west of the Hersek delta and a segment along the trace of the 12 November Düzce rupture east of the İzmit rupture. Whereas the coseismic fault slip occurred in the upper 15–20 km of the crust (Reilinger *et al.*, 2000), the postseismic slip model allows for slip deep into the lower crust and upper mantle to a depth of 50 km. To evaluate the spatial distribution of afterslip, we further subdivide the discontinuous fault surface into approximately 4.5- by 4.2-km sized patches. We invert for the optimal slip distribution on these fault elements and seek models that minimize the data misfit, while preserving smoothness of the model slip distribution. We expand the strike-slip distribution in spatial basis functions (Segall *et al.*, 2000), which are chosen to minimize the roughness of the slip function in addition to seeking a good fit to the data. The roughness is measured by $|\nabla^2\mathbf{u}(x)|$, where $\mathbf{u}(x)$ is the vector of fault slips and ∇^2 is a finite-difference approximation of the Laplacian operator (Harris and Segall, 1987). We include the first 12 basis functions (including an initial

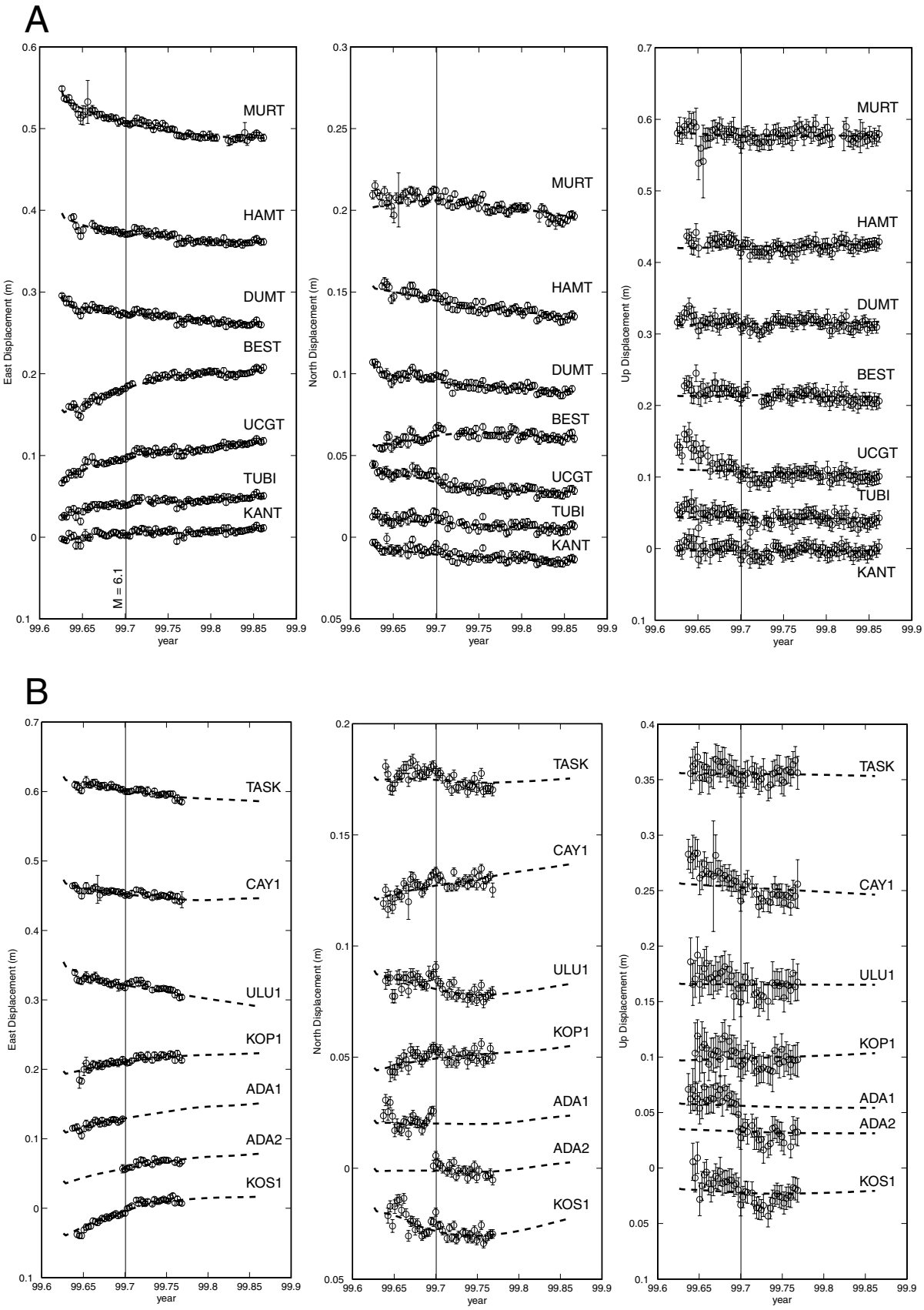

Figure 2. Caption on facing page.

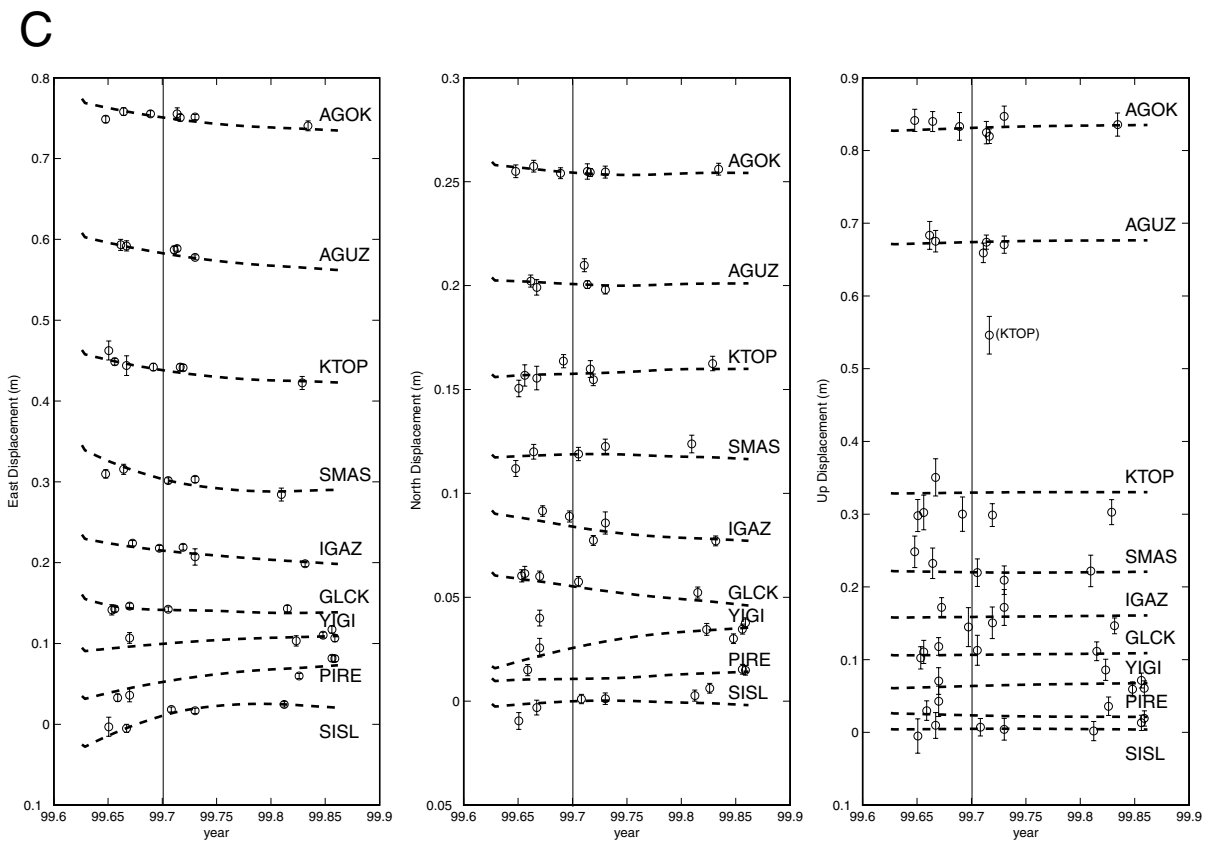

Figure 2. Time series of east, north, and vertical coordinate components of the GPS stations that were occupied at least 5 times between 17 August and 11 November 1999. The time series are shown relative to a site in Graz, Austria, that is located deep within Eurasia. Dashed bold lines indicate predicted displacements from the time-dependent slip inversion of the postseismic GPS data (Fig. 5). The depicted time series are not corrected for secular motions, however, the maximum correction applied to the data for the modeling is a ca. 5 mm eastward motion, which is about the size of the circles marking the data points. Curves have been offset vertically for clarity. Thin vertical lines indicate the time of the largest, 13 September M_w 5.8 aftershock. (A) Continuously and semicontinuously operating sites of the Marmara GPS monitoring network; (B) GFZ network sites; (C) campaign survey sites observed at least 5 times during the observation period. The large outlier in the vertical component of station KTOP is likely to represent a setup error.

uniform-slip solution), and the inverted slip distribution is made up of time-varying, linear combinations of these functions (Fig. 4). Slip models of shorter wavelength than the highest-order basis functions cannot appear in the solution. The lower-order basis functions are relatively insensitive to the data distribution, whereas the coefficients of the higher-order terms can become very small because of the damping imposed by the spatial smoothing (Segall *et al.,* 2000). A comparison of our eventual slip models with the basis functions shows that the higher-order basis functions do not appear in the solution, as the data distribution does not warrant such complex models.

The model fault extends well below and to the west and the east, beyond the coseismic rupture. We apply edge constraints to favor models that minimize slip on the western and easternmost and top and bottom edges of the discontinuous fault model. We justify the no-slip constraint along the top row of fault elements by the lack of observations of any notable surficial creep following the İzmit earthquake.

Spatial and temporal variations in fault slip are modeled simultaneously using the observed GPS positions and covariances of the full network. The NIF requires a choice of temporal (α) and spatial (γ) smoothing parameters, as well as the determination of the magnitude of bench mark random walk (τ) and a scale factor by which the formal errors of the GPS solution might need to be multiplied (Segall *et al.*, 2000). Here, we adopt a bench mark random walk scale parameter of τ equals 2 mm/yr$^{1/2}$, which seems to be representative of standard monuments (Langbein and Johnson, 1997), and apply no further scaling of the data covariance as the observed repeatability of the data is consistent with the observation errors. Solutions with γ equal to 0 and α

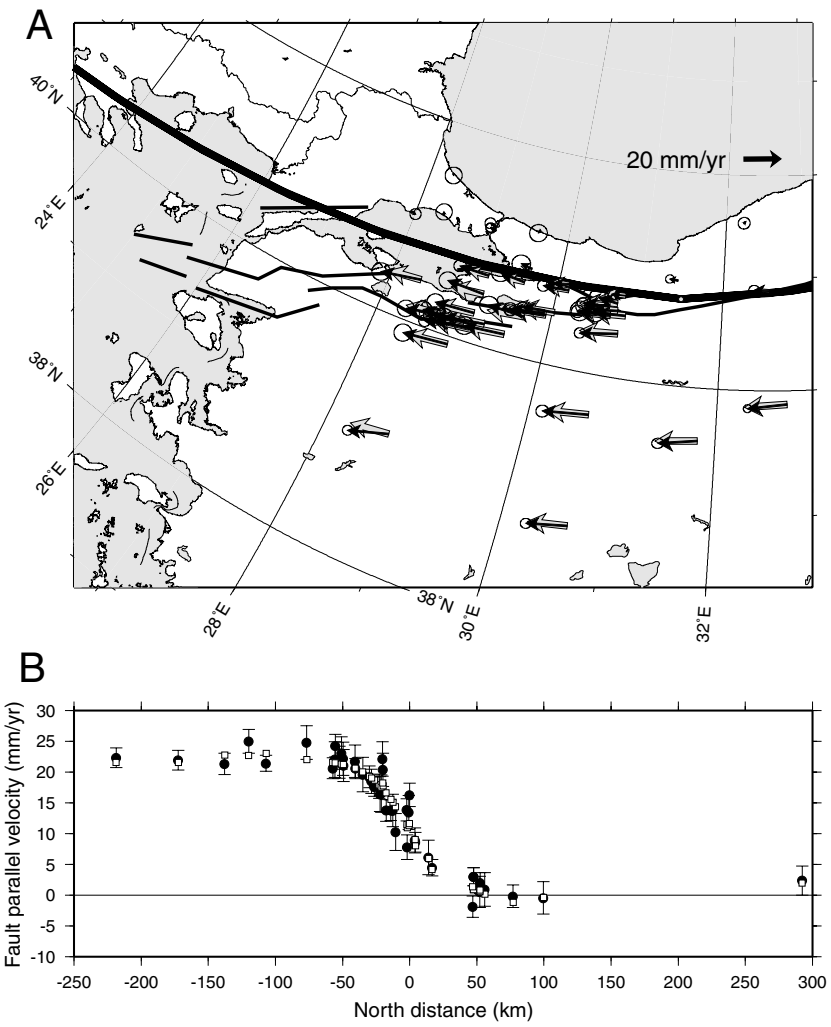

Figure 3. Secular dislocation model fit to interseismic GPS velocities (solid arrows tipped with 95% error ellipses) of 45 GPS sites (McClusky *et al.,* 2000) located between 28° E and 33° E and between 38.5° N and 42° N. This model is used to correct postseismic GPS observations for steady background motions. (A) Map is in oblique Mercator projection about the Anatolia–Eurasia angular rotation pole (McClusky *et al.,* 2000) so that horizontal lines and velocity vectors are parallel to the relative plate motion. The trend of the NAF significantly diverges from that of a small circle about the rotation pole indicating a significant extensional component in the Sea of Marmara region (McClusky *et al.,* 2000). Bold line indicates the single straight dislocation plane buried below 24.4 km depth and slipping at 32 mm/yr that produces the model velocities shown as open arrows. (B) Observed (solid circles with 1-sigma error bars) and modeled (open circles) fault parallel velocities.

equal to 0 correspond to spatially uniform slip-rate and temporally steady slip-rate models, respectively. Increasing γ allows for more complex slip distributions to improve the model fit, whereas increasing α improves the fit to the data by increasing the temporal complexity of the model. We initially estimate the filter hyperparameters for temporal and spatial smoothing, α and γ, by maximum likelihood (Segall and Matthews, 1997; Segall *et al.*, 2000). We numerically calculate the likelihood for a range of α and γ to find the optimal solution that fits the data well while not becoming unnecessarily complex. The maximum likelihood analysis suggests values of 47 and 0.02 for α and γ, respectively (Fig. 5).

The NIF model inversions indicate that large amounts of right-lateral strike slip occurred during the observation period; however, the models commonly include some left-lateral slip. It might be possible that some postseismic afterslip, opposite to the coseismic slip, occurs in areas where dynamic slip overshoot occurred. However, we believe that the left-lateral slip patches in the model are an artifact of the inversion that reflects the limits of resolution. Left-lateral slip is not currently penalized (by nonnegativity constraints) in the NIF inversion. We compute over the same range of smoothing-parameter values, for which we derived maximum likelihood values, the sum of the accumulated left-lateral slip on each fault element multiplied by fault patch area and rigidity, corresponding to the total geodetic moment of left-lateral slip (Fig. 5). Left-lateral slip is minimized with the lowest values of α and γ in our grid search. To avoid large amounts of left-lateral slip in our model, we require more smoothing than indicated by the maximum likelihood analysis, and we use α equal to 4 and γ equal to 0.1 in our final inversions. The weighted residual sum of squares divided by the number of data N (3708 GPS coordinate observations) in our final model is 1.23 versus 1.05 in the maximum likelihood solution. Small amounts of left-lateral slip still occur in our final model in areas not well constrained by our GPS network but do not substantially affect our result.

Inversion Results

Using all the GPS-measured site positions corrected for secular deformation in the region, the model geometry, and NIF model parameters as described in the previous section, we compute our favored model of transient distributed

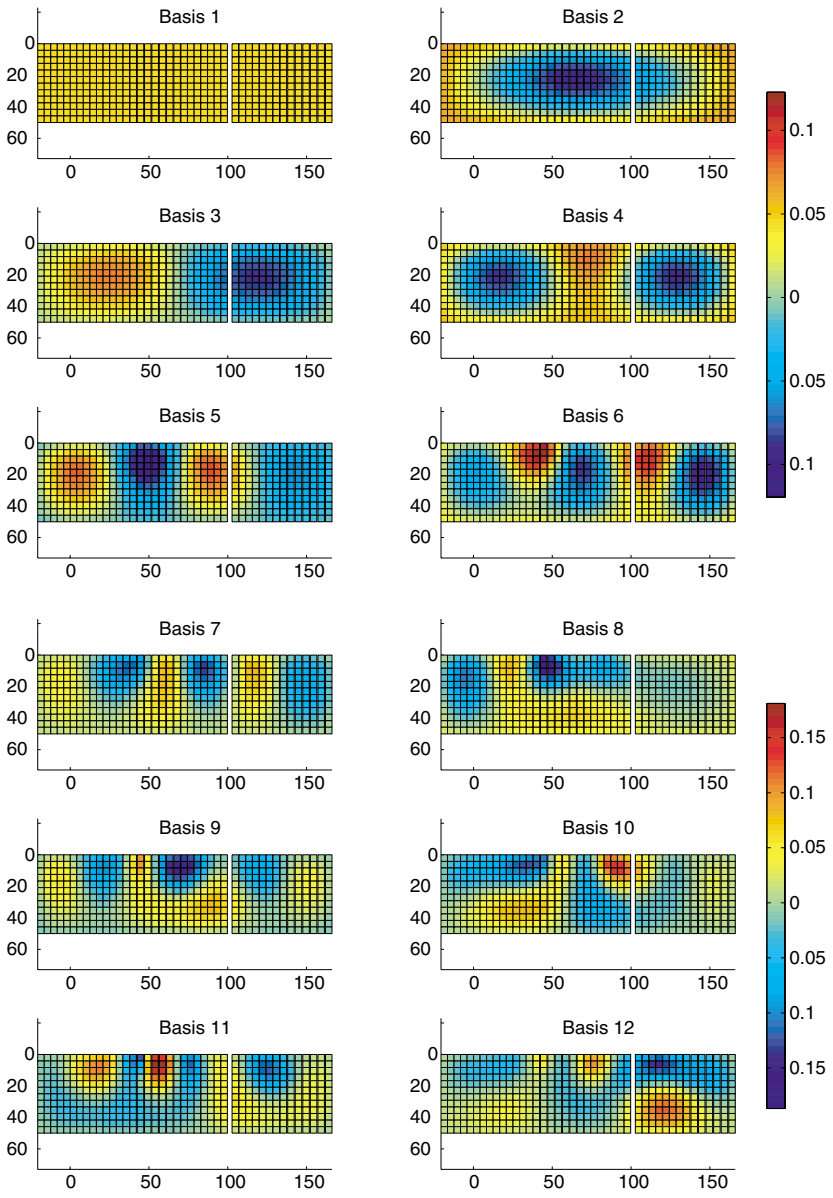

Figure 4. The first 12 basis functions for strike slip on the segmented, vertical afterslip fault plane including the Yalova and Düzce fault segments adjacent to the coseismic rupture. Each plot shows the ca. 180-km by 50-km segmented fault plane viewed from the south. The estimated slip-rate distribution is a linear combination of these functions, with coefficients that vary in time such as to fit the GPS data.

afterslip. Figure 6 shows eight snapshots of the slip rate at 10-day intervals following the İzmit earthquake. An animated version of the slip rate model can be viewed at *http://www.seismo.berkeley.edu/~burgmann/RESEARCH/research.html.* Two large afterslip patches are apparent near the İzmit earthquake hypocenter and at depth along the Karadere rupture segment. Figure 7 shows the time-dependent station displacements computed from this model. Figure 8 shows cumulative slip as a function of time at about 10 km and at 35 km depths below the epicenter and near the center of the Karadere segment. Shallow afterslip near the hypocenter at ca. 30° E (54.4 km distance in Fig. 6) rapidly decayed within about 30 days, whereas deep afterslip continued at undiminished rates at Moho depths.

Shallow afterslip along the Karadere segment was small and decayed rapidly to near-zero rates (Figs. 6 and 8). The maximum afterslip is inferred deep below the Karadere fault segment, which continued until the time of the subsequent Düzce rupture, immediately to the east. Maximum afterslip occurred at rates of up to 2.2 m/yr for a total of 0.4 m. Afterslip in the last month of the observation period appears restricted to depths greater than 12–16 km; that is, it occurred below the coseismic rupture plane. Slip occurs all the way to the bottom of the 50-km-wide model fault, only limited by the bottom-edge constraint in the inversion. This suggests that rapid afterslip occurred at least down to the Moho at ca. 35 km depth and possibly into the upper mantle.

The model fits the longer temporal wavelength patterns in the observed displacements well (Fig. 2). Some higher-frequency signal is apparent in the continuous station data that the model does not attempt to match, in the interest of spatial and temporal model smoothness. Some features, such as the apparent large subsidence of UCGT (Fig. 2A) during the first postseismic month are not captured by the model,

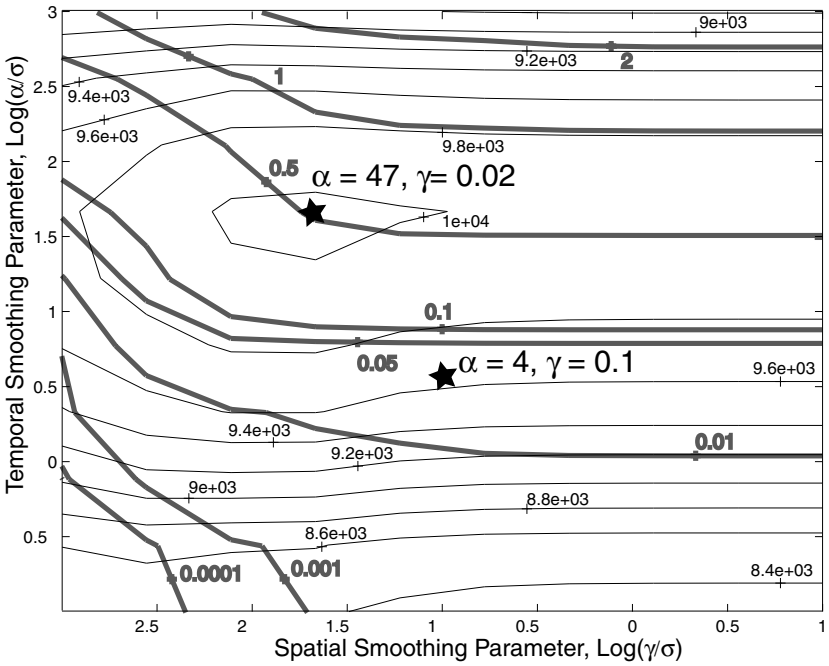

Figure 5. Maximum likelihood analysis to determine the temporal smoothing parameter α and the spatial smoothing parameter γ. The minus twice the logarithm of likelihood contour surface (thin black contour lines) is shown as a function of $\log_{10}(\alpha)$ and $\log_{10}(\gamma)$. The maximum likelihood estimate is indicated by a star ($\alpha = 47$ and $\gamma = 0.02$). Bold gray contours indicate the left-lateral (opposite to expected NAF motion) moment ($\times 10^{19}$ N m) of the respective afterslip models. In the final inversions we choose values of α equal to 4 and γ equal to 0.1 to avoid models that involve large amounts of left-lateral afterslip.

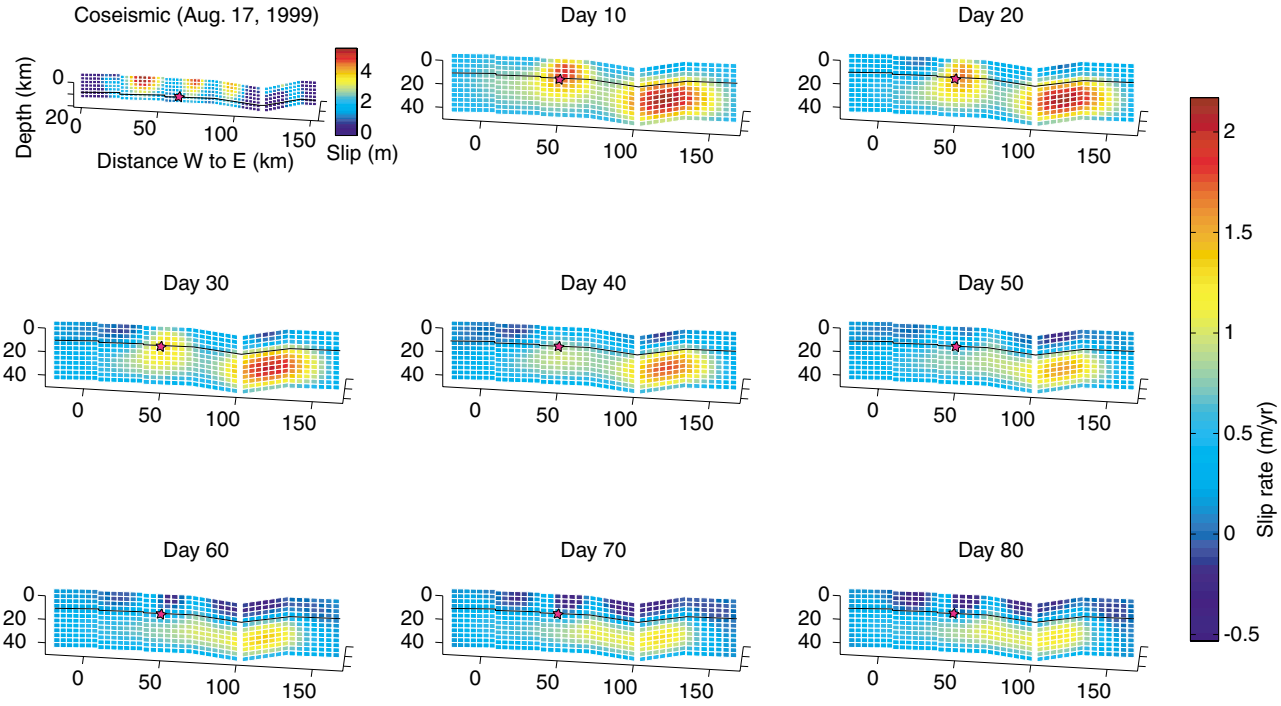

Figure 6. Top left panel shows coseismic slip model inverted from GPS measurements (modified from Reilinger *et al.,* 2000). Remaining panels show snapshots of time-dependent distributed strike-slip rate inverted from the postseismic GPS measurements in 10-day intervals. Following rapid slip over a large portion of the model fault early on, most slip occurs down-dip of the coseismic rupture, with the upper ca. 12–16 km (3–4 fault patches) devoid of significant slip. The location of the 17 August hypocenter is indicated by pink stars. A black line indicates the depth of the base of the seismogenic zone (~16 km) inferred from the coseismic slip distribution and depth of microseismicity in the area. With time, slip apparently propagates downward and laterally away from the central fault segment near the hypocenter (~50 km distance). The highest slip is inferred below the Karadere fault segment (100–130 km distance), immediately west of the eventual Düzce rupture.

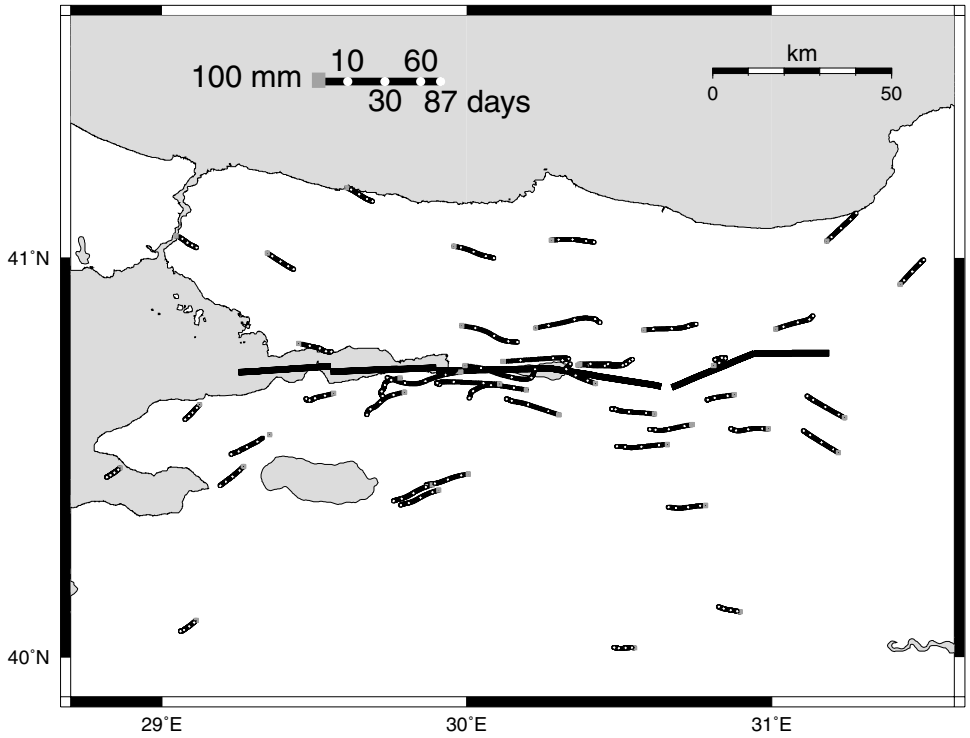

Figure 7. Map of time-dependent model station displacements. Gray squares indicate the station position from which the motions are shown in 1-day increments. White circles indicate the site positions at 10, 30, 60, and 87 days, as indicated on the displacement scale bar. The bold line indicates the surface projection of the fault geometry used in the model inversions.

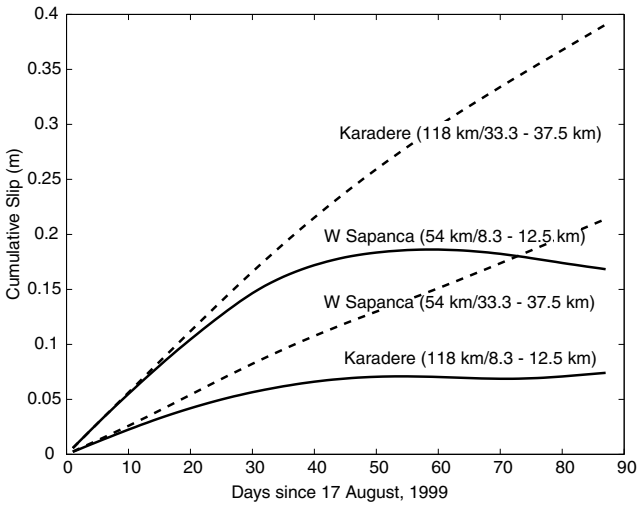

Figure 8. Slip histories on dislocation elements near the hypocenter along the western Sapanca segment (West Sapanca near 30° E) and near the center of the Karadere rupture segment (near 30.9° E). Cumulative afterslip is shown for patches at seismogenic depths in the upper crust (8.33–12.5 km, solid lines) and near the base of the crust (33.3–37.5 km, dashed lines). Along-fault distances in labels are shown in Figure 6.

and we recognize some apparent outliers, such as the 20-cm vertical offset of a measurement at KTOP (Fig. 2C).

Discussion and Conclusions

The GPS measurements after the 17 August 1999 İzmit earthquake show rapid transient deformation during the 87-day period leading to the subsequent 11 November Düzce earthquake. Formal model inversion of the data for spatially and temporally variable afterslip suggests that the first phase of postseismic deformation was caused by rapid (up to 2.2 m/yr) slip on and below the coseismic rupture. The cumulative geodetic moment during the 87-day period was M_0 4.47×10^{19} Nm, the equivalent of an M_w 7.1 earthquake. This is about an order of magnitude more than the moment released by the aftershocks of the İzmit earthquake (Ergintav *et al.*, 2002). The upper crustal afterslip appears localized in the regions in which dynamic slip was impeded such as around the hypocenter and below ca. 6 km depth along the Karadere segment. Shallow afterslip decayed rapidly within about 1 month, whereas slip deep below the rupture continued until the time of the Düzce event. Rapid slip at depth, in particular below the eastern Karadere rupture segment, added to the coseismic static stress changes on the neighboring Düzce earthquake rupture, which failed about 3 months after the İzmit event (Hearn *et al.*, 2002).

Our inversion for slip distributions in an elastic halfspace assume that deformation is caused by localized shear on the coseismic rupture and its down-dip extension deep into the lithosphere. To explain this deformation with distributed viscous flow in the crust, a viscosity of ca. 4×10^{17} Pa sec is required for the lower crust (Hearn *et al.*, 2002). Such values are 2–4 orders of magnitude below the range of most previous estimates of crustal viscosity based on the deformation measurements and experimental data. Temperatures of 700°–950°C or more would be required in the midcrust to lower crust to achieve adequate effective viscosities in typical crustal rock types that can explain transients of a few months duration (Ivins, 1996, 2000). We note that both the spatial pattern as well as the rapidly decaying nature of the deformation are not consistent with deformation rates expected from viscous relaxation of a broadly deforming lower crust (Hearn *et al.* 2002).

As the zone of postseismic afterslip overlaps significantly with the inferred locking depth of ca. 17 km in the years before the earthquake (Meade *et al.*, 2002), our observations are consistent with an earthquake cycle model for the western North Anatolian fault zone in which (1) steady interseismic deformation occurs in the lower crust and underlying mantle lithosphere accommodated by localized shear and distributed ductile flow; (2) aseismic faulting occurs at midcrustal to lower crustal levels, which is highly accelerated following the sudden stress pulse from the İzmit earthquake; and (3) brittle seismic faulting occurs in the upper crust followed by localized afterslip along some portions of the rupture. This model is consistent with the experimental (Blanpied *et al.,* 1991) and theoretical studies (Tse and Rice, 1986) of a velocity-strengthening fault zone rheology at depth, as well as some seismic studies that imaged a narrow down-dip extension along the San Andreas fault (Henstock *et al.*, 1997; Parsons, 1998; Zhu, 2000). However, this does not rule out distributed viscous relaxation in the surrounding lower crust and upper mantle in the years to come (e.g., Pollitz *et al.*, 2000). We conclude that the postseismic deformation following the İzmit earthquake indicates a narrow, velocity-strengthening fault zone extending through the crust and possibly into the upper mantle.

Acknowledgments

This research was supported in part by NSF grants to MIT EAR-9909730 and INT-9909619 and a grant by the World Bank to TUBITAK MRC. Part of the GPS data were collected by the German Task Force for Earthquakes sponsored by the GFZ and the Hannover Re. We thank Jeff Freymueller for his careful review, which helped us improve the article. R.B. thanks his colleagues at MIT for their hospitality during a sabbatical semester at the Department of Earth, Atmospheric, and Planetary Sciences. This is Berkeley Seismological Laboratory contribution 02-01.

References

Aoki, Y., P. Segall, T. Kato, P. Cervelli, and S. Shimada (1999). Imaging magma transport during the 1997 seismic swarm off the Izu Peninsula, Japan, *Science* **286,** 927–930.

Ayhan, M. E., R. Bürgmann, S. McClusky, O. Lenk, B. Aktug, E. Herece, and R. E. Reilinger (2001). Kinematics of the $M_w = 7.2$, 12 November 1999, Düzce, Turkey Earthquake, *Geophys. Res. Lett.* **28,** 367–370.

Bak, J., J. Korstgard, and K. Sorensen (1975). A major shear zone within the Nagssugtoqidian of west Greenland, *Tectonophysics* **27,** 191–209.

Blanpied, M. L., D. A. Lockner, and J. D. Byerlee (1991). Fault stability inferred from granite sliding experiments at hydrothermal conditions, *Geophys. Res. Lett.* **18,** 609–612.

Bourne, S. J., P. C. England, and B. Parsons (1998). The motion of crustal blocks driven by flow of the lower lithosphere and implications for slip rates of continental strike-slip faults, *Nature* **391,** 655–659.

Brocher, T. M., J. McCarthy, P. E. Hart, W. S. Holbrook, K. P. Furlong, T. V. McEvilly, J. A. Hole, and S. L. Klemperer (1994). Seismic evidence for a lower-crustal detachment beneath San Francisco Bay, California, *Science* **265,** 1436–1439.

Bürgmann, R., M. E. Ayhan, E. J. Fielding, T. Wright, S. McClusky, B. Aktug, C. Demir, O. Lenk, and A. Türkezer (2002). Deformation during the 12 November 1999, Düzce, Turkey Earthquake, from GPS and InSAR Data, *Bull. Seism. Soc. Am.* **92,** no. 1, 161–171.

Bürgmann, R., P. Segall, M. Lisowski, and J. Svarc (1997). Postseismic strain following the 1989 Loma Prieta earthquake from GPS and leveling measurements, *J. Geophys. Res.* **102,** 4933–4955.

Deng, J., M. Gurnis, H. Kanamori, and E. Hauksson (1998). Viscoelastic flow in the lower crust after the 1992 Landers, California, earthquake, *Science* **282,** 1689–1692.

Dong, D., T. A. Herring, and R. W. King (1998). Estimating regional deformation from a combination of space and terrestrial geodetic data, *J. Geod.* **72,** 200–211.

Donnellan, A., and G. A. Lyzenga (1998). GPS observations of fault afterslip and upper crustal deformation following the Northridge earthquake, *J. Geophys. Res.* **103,** 21,285–21,297.

Ergintav, S., R. Bürgmann, S. McClusky, *et al.* (2002). Postseismic deformation near the İzmit earthquake (17 August 1999, *M* 7.5) rupture zone, *Bull. Seism. Soc. Am.* **92,** no. 1, 194–207.

Furlong, K. P., and D. Verdonck (1994). Three-dimensional lithospheric kinematics in the Loma Prieta region, California: implications for the earthquake cycle, *U.S. Geol. Surv. Profess. Pap.* **1550-F,** 103–131.

Gilbert, L. E., C. H. Scholz, and J. Beavan (1994). Strain localization along the San Andreas fault: consequences for loading mechanisms, *J. Geophys. Res.* **99,** 23,975–23,984.

Hanmer, S. (1988). Great Slave Lake shear zone, Canadian shield: reconstructed vertical profile of a crustal-scale fault zone, *Tectonophysics* **149,** 245–264.

Harris, R., and P. Segall (1987). Detection of a locked zone at depth on the Parkfield, California segment of the San Andreas fault, *J. Geophys. Res.* **92,** 7945–7962.

Hearn, E. H., R. Bürgmann, and R. Reilinger (2002). Dynamics of İzmit earthquake postseismic deformation and loading of the Düzce earthquake hypocenter, *Bull. Seism. Soc. Am.* **92,** no. 1, 172–193.

Henstock, T. J., A. Levander, and J. A. Hole (1997). Deformation in the lower crust of the San Andreas fault system in northern California, *Science* **278,** 650–653.

Herring, T. A. (1999). GLOBK: Global Kalman filter VLBI and GPS analysis program Version 5.9, Massachusetts Institute of Technology, Cambridge, Massachusetts.

Hubert-Ferrari, A., A. Barka, B. Jacques, S. S. Nalbant, B. Moyer, B. Armijo, P. Topponier, and G. C. P. King (2000). Seismic hazard in the Marmara Sea region following the 17 August 1999 İzmit earthquake, *Nature* **404,** 269–272.

Ivins, E. R. (1996). Transient creep of a composite lower crust 2: a polymineralic basis for rapidly evolving postseismic deformation modes, *J. Geophys. Res.* **101,** 28,005–28,028.

Ivins, E. R. (2000). Correction to "Transient creep of a composite lower crust 2: a polymineralic basis for rapidly evolving postseismic deformation modes" by Erik R. Ivins, *J. Geophys. Res.* **105,** 3229–3231.

King, R. W., and Y. Bock (1998). Documentation for the GAMIT analysis

software, release 9.7, Massachusetts Institute of Technology, Cambridge, Massachusetts.

Langbein, J., and H. Johnson (1997). Correlated errors in geodetic time series: implications for time-dependent deformation, *J. Geophys. Res.* **102,** 591–603.

Lehner, F. K., V. C. Li, and J. R. Rice (1981). Stress diffusion along rupturing plate boundaries, *J. Geophys. Res.* **86,** 6155–6169.

Makris, J., and C. Stobbe (1984). Physical properties and state of the crust and upper mantle of the eastern Mediterranean Sea deduced from geophysical data, *Marine Geol.* **55,** 347–363.

McClusky, S., S. Balassanian, A. Barka, C. Demir, S. Ergintav, I. Georgiev, O. Gurkan, M. Hamburger, K. Hurst, H. Kahle, *et al.* (2000). Global Positioning System constraints on plate kinematics and dynamics in the eastern Mediterranean and Caucusus, *J. Geophys. Res.* **105,** 5695–5720.

Meade, B., B. Hager, S. McClusky, R. Reilinger, S. Ergintav, O. Lenk, A. Barka, and H. Ozener (2002). Estimates of seismic potential in the Marmara Sea region from block models of secular deformation constrained by global positioning system measurements, *Bull. Seism. Soc. Am.* **92,** no. 1, 208–215.

Molnar, P., H. J. Anderson, E. Audoine, D. Eberhart-Phillips, K. R. Gledhill, E. R. Kloska, T. V. McEvilly, D. Okaya, M. K. Savage, T. Stern, *et al.* (1999). Continuous deformation versus faulting through the continental lithosphere of New Zealand, *Science* **286,** 516–519.

Nur, A., and G. Mavko (1974). Postseismic viscoelastic rebound, *Science* **183,** 204–206.

Okada, Y. (1985). Surface deformation due to shear and tensile faults in a half-space, *Bull. Seism. Soc. Am.* **75,** 1135–1154.

Parsons, T. (1998). Seismic-reflection evidence that the Hayward fault extends into the lower crust of the San Francisco Bay area, California, *Seism. Soc. Am. Bull.* **88,** 1212–1223.

Parsons, T., S. Toda, R. S. Stein, A. Barka, and J. H. Dietrich (2000). Heightened odds of large earthquakes near Istanbul: an interaction-based probability calculation, *Science* **288,** 661–665.

Pollitz, F. F. (1992). Postseismic relaxation theory on the spherical earth, *Bull. Seism. Soc. Am.* **82,** 422–453.

Pollitz, F., R. Bürgmann, and P. Segall (1998). Joint estimation of afterslip rate and postseismic relaxation following the 1989 Loma Prieta earthquake, *J. Geophys. Res.* **103,** 26,975–26,992.

Pollitz, F. F., G. Peltzer, and R. Bürgmann (2000). Mobility of continental mantle: evidence from postseismic geodetic observations following the 1992 Landers earthquake, *J. Geophys. Res.* **105,** 8035–8054.

Prescott, W. H., and S.-B. Yu (1986). Geodetic measurement of horizontal deformation in the northern San Francisco Bay region, California, *J. Geophys. Res.* **91,** 7475–7484.

Reilinger, R. E., S. Ergintav, R. Bürgmann, S. McClusky, O. Lenk, A. Barka, O. Gurkan, L. Hearn, K. L. Feıgl, R. Cakmak, *et al.* (2000). Coseismic and postseismic fault slip for the 17 August 1999, M = 7.5, İzmit, Turkey earthquake, *Science* **289,** 1519–1524.

Savage, J. C. (1990). Equivalent strike-slip earthquake cycles in half-space and lithosphere-asthenosphere earth models, *J. Geophys. Res.* **95,** 4873–4879.

Savage, J. C., and J. L. Svarc (1997). Postseismic deformation associated with the 1992 M_w = 7.3 Landers earthquake, southern California, *J. Geophys. Res.* **102,** 7565–7577.

Scholz, C. H. (1988). The brittle-plastic transition and the depth of seismic faulting, *Geol.Rdsch.* **77,** 319–328.

Segall, P., and M. Matthews (1997). Time dependent inversion of geodetic data, *J. Geophys. Res.* **103,** 22,391–22,409.

Segall, P., R. Bürgmann, and M. Matthews (2000). Time dependent deformation following the 1989 Loma Prieta earthquake, *J. Geophys. Res.* **105,** 5615–5634.

Shen, Z. K., D. D. Jackson, Y. Feng, *et al.* (1994). Postseismic deformation following the Landers earthquake, California, 28 June 1992, *Bull. Seism. Soc. Am.* **84,** 780–791.

Sibson, R. H. (1986). Earthquakes and rock deformation in crustal fault zones, *Ann. Rev. Earth Planet. Sci.* **14,** 149–175.

Stein, R. S., A. A. Barka, and J. H. Dietrich (1997). Progressive failure on the North Anatolian fault since 1939 by earthquake stress triggering, *Geophys. J. Int.* **128,** 594–604.

Straub, C., H.-G. Kahle, and C. Schindler (1997). GPS and geologic estimates of the tectonic activity in the Marmara Sea region, NW Anatolia, *J. Geophys. Res.* **102,** 27,587–27,601.

Swanson, M. T. (1992). Fault structure, wear mechanisms and rupture processes in pseudotachylyte generation, *Tectonophysics* **204,** 223–242.

Thatcher, W. (1974). Strain release mechanism of the 1906 San Francisco earthquake, *Science* **184,** 1283–1285.

Thatcher, W. (1983). Nonlinear strain buildup and the earthquake cycle on the San Andreas fault, *J. Geophys. Res.* **88,** 5893–5902.

Toksöz, M. N., A. F. Shakal, and A. J. Michael (1979). Space-time migration of earthquakes along the North Anatolian fault zone and seismic gaps, *Pageoph* **117,** 1258–1270.

Tse, S. T., and J. R. Rice (1986). Crustal earthquake instability in relation to the depth variation of frictional slip properties, *J. Geophys. Res.* **91,** 9452–9472.

Woith, H., J. Zschau, and R. Yilmaz (1999). Multidisciplinary investigations of the German earthquake task force following the İzmit M_w = 7.6 earthquake of August 17, 1999, and the Düzce M_w = 7.0 event of November 12, 1999, *EOS, Trans. Am. Geophys. U.* **80,** 663.

Yang, M., and M. N. Toksöz (1981). Time-dependent deformation and stress relaxation after strike-slip earthquakes, *J. Geophys. Res.* **86**, 2889–2901.

Zhu, L. (2000). Crustal structure across the San Andreas fault, southern California from teleseismic converted waves, *Earth Planet. Sci. Lett.* **179**, 183–190.

Department of Earth and Planetary Science and Berkeley Seismological Laboratory
307 McCone Hall
University of California, Berkeley
Berkeley, California 94720
burgmann@seismo.berkeley.edu
(R.B.)

TUBITAK
Marmara Research Center, ESRI
Gebze 41470
Turkey
(S.E.)

Department of Geophysics
Stanford University
Stanford California 94503
(P.S.)

Department of Earth, Atmospheric, and Planetary Sciences
Massachusetts Institute of Technology
E34, 42 Carleton Street
Cambridge, Massachusetts 02142
(E.H.H., S.M., R.E.R.)

GeoForschungsZentrum Potsdam
Telegrafenberg
D-14473 Potsdam
Germany
(H.W., J.Z.)

Manuscript received 22 September 2000.